Available online at www.sciencedirect.com
ScienceDirect
Journal of Computational Physics 227 (2007) 1544–1566
JOURNAL OF COMPUTATIONAL PHYSICS
www.elsevier.com/locate/jcp

Poloidal–toroidal decomposition in a finite cylinder II. Discretization, regularization and validation

Piotr Boronski *, Laurette S. Tuckerman

LIMSI-CNRS, BP 133, 91403 Orsay, France

Received 7 May 2007; received in revised form 25 August 2007; accepted 28 August 2007
Available online 14 September 2007

Abstract

The Navier–Stokes equations in a finite cylinder are written in terms of poloidal and toroidal potentials in order to impose incompressibility. Regularity of the solutions is ensured in several ways: First, the potentials are represented using a spectral basis which is analytic at the cylindrical axis. Second, the non-physical discontinuous boundary conditions at the cylindrical corners are smoothed using a polynomial approximation to a steep exponential profile. Third, the nonlinear term is evaluated in such a way as to eliminate singularities. The resulting pseudo-spectral code is tested using exact polynomial solutions and the spectral convergence of the coefficients is demonstrated. Our solutions are shown to agree with exact polynomial solutions and with previous calculations of axisymmetric vortex breakdown and of onset of non-axisymmetric helical spirals. Parallelization by azimuthal wavenumber is shown to be highly effective.
© 2007 Elsevier Inc. All rights reserved.

Keywords: Cylindrical coordinates; Coordinate singularities; Pseudo-spectral; Recursion relations; Radial basis; Vortex breakdown; Spectral convergence; Poloidal–toroidal; Finite cylinder

1. Introduction

The von Kármán flow owes its name to von Kármán [1] who in 1921 first studied the flow in the semi-infinite domain bounded by a single rotating disk using a similarity transformation. In 1951, Batchelor [2] extended the problem to the flow confined between two infinite rotating disks. For rotating disks of finite radius, the configuration can be described by three control parameters: the ratio s of the angular velocity of the two disks, the height-to-radius ratio h and a Reynolds number Re based on the radius and the azimuthal velocity of one of the disks. The variation of these three parameters (Re, s, h) has proved to yield a rich variety of qualitatively different accessible flows, even before the onset of turbulence. The symmetries influence the transitions that the flow can undergo. This configuration is extensively studied in the context of transition to complex and turbulent flows. All of these properties explain why the von Kármán flow is increasingly

DOI of original article: 10.1016/j.jcp.2007.08.023.
* Corresponding author.
E-mail address: boronski@gmail.com (P. Boronski).

0021-9991/$ - see front matter © 2007 Elsevier Inc. All rights reserved.
doi:10.1016/j.jcp.2007.08.035

considered as one of the classical hydrodynamic configurations and why the scientific community is interested in further exploring its complex behavior.

The first numerical studies were necessarily devoted to axisymmetric flows and their stability. In the rotor–stator configuration ($s = 0$), vortex breakdown forming characteristic recirculation bubbles was observed by Lugt and Abboud [3], Daube and Sorensen [4], Lopez [5] and Daube [6]. This now well-documented configuration has become a benchmark for testing axisymmetric codes. Following Lopez and Shen [7], Speetjens and Clercx [8] and a number of other authors, we will validate our method in the axisymmetric configuration by reproducing the stationary state at $Re = 1800$ and the oscillating flow at $Re = 2800$, for which we will compare the bifurcation threshold and the oscillation frequency against previous findings.

Increasing computational power has made it possible to study three-dimensional instabilities. Breaking of axisymmetry has been the subject of several studies, of which we mention those of Gauthier et al. [9], Gelfgat et al. [10], Blackburn and Lopez [11], Lopez et al. [12] and Nore et al. [13]. Three-dimensional instability precedes axisymmetric instability for $h < 1.6$ and $h > 2.8$. As the test problem for validating our code in three dimensions, we have selected a configuration with $s = -1$, $h = 3.5$, $Re = 2150$, where the deviation from the axisymmetric flow takes the form of a helical spiral. In Section 3.5 we compare our results with those of Lopez et al. [14] and Gelfgat et al. [10].

Interesting phenomena can also be observed in the turbulent regime. Turbulence may coexist with and large-scale structures. In experiments in a turbulent counter-rotating configuration, Marié [15] and Ravelet et al. [16] discovered that a two-cell mean flow with a shear layer at the cylinder mid-plane undergoes switching to a one-cell mean flow whose shear layer is adjacent to the less rapidly rotating disk. This transition can be observed at Reynolds numbers which are numerically accessible.

A comprehensive classification of the solutions for different values of the parameters (s, h, Re) is beyond the scope of this work. Our main purpose here is to develop a mathematical and algorithmic tool which can be applied to von Kármán flow and to rotating turbulence, and which can be extended to the magnetohydrodynamic configuration of the VKS experiment [17]. The major component of our algorithm is the poloidal–toroidal decomposition [18,19], which insures incompressibility by construction, at the price of increasing the order of the governing equations. When applied to the Navier–Stokes equation in a finite cylinder, the resulting system has boundary conditions which are coupled and of high order. In a companion article [20], we showed that this system could be reduced to the solution of a set of nested Helmholtz and Poisson problems with uncoupled Dirichlet boundary conditions, whose solutions could be superposed via the influence matrix technique. The purpose of the present article is to describe our method for solving these elliptic problems using a spectral representation which exploits the azimuthal symmetry of the system and which is regular at the cylindrical axis, and to demonstrate the validity of the resulting hydrodynamic code.

More specifically, it was shown by Marques and co-workers [18,19] that the Navier–Stokes equations

$$\partial_t \mathbf{u} + (\mathbf{u}\cdot\nabla)\mathbf{u} = Re^{-1}\Delta\mathbf{u} - \nabla p \tag{1.1a}$$

$$\nabla\cdot\mathbf{u} = 0 \tag{1.1b}$$

in a finite cylinder with boundary conditions

$$\mathbf{u} = r\omega_{\pm}\hat{\mathbf{e}}_\theta \quad \text{at } z = \pm\frac{h}{2} \tag{1.2a}$$

$$\mathbf{u} = 0 \qquad \text{at } r = 1, \tag{1.2b}$$

and with toroidal and poloidal potentials defined by

$$\mathbf{u} = \nabla\times(\psi\hat{\mathbf{e}}_z) + \nabla\times\nabla\times(\phi\hat{\mathbf{e}}_z) \tag{1.3}$$

are equivalent to the two scalar equations

$$(\partial_t - Re^{-1}\Delta)\Delta_h\psi = S_\psi \equiv \hat{\mathbf{e}}_z\cdot\nabla\times(\mathbf{u}\cdot\nabla)\mathbf{u} \tag{1.4a}$$

$$(\partial_t - Re^{-1}\Delta)\Delta\Delta_h\phi = S_\phi \equiv -\hat{\mathbf{e}}_z\cdot\nabla\times\nabla\times(\mathbf{u}\cdot\nabla)\mathbf{u} \tag{1.4b}$$

where $\Delta_h \equiv \frac{1}{r}\partial_r r \partial_r + \frac{1}{r^2}\partial_\theta^2$, with boundary conditions

$$\frac{1}{r}\partial_\theta\psi + \partial_{rz}\phi = \partial_r\psi = \Delta_h\phi = \phi = \partial_{rz}\Delta_h\psi - \frac{1}{r}\partial_\theta\Delta\Delta_h\phi = 0 \quad \text{at } r = 1 \tag{1.5a}$$

$$\psi = 0 \quad \text{at } r = 0 \tag{1.5b}$$

$$\Delta_h\psi + \frac{1}{r}\partial_r\left(\omega_\pm r^2\right) = \partial_z\Delta_h\phi = \Delta_h\phi = 0 \quad \text{at } z = \pm\frac{h}{2} \tag{1.5c}$$

Our article [20] was devoted to showing how the problem (1.4) and (1.5) can in turn be reduced to a sequence of five nested parabolic and elliptic problems, each with Dirichlet boundary conditions:

$$\left(\partial_t - Re^{-1}\Delta\right)f_\psi = S_\psi, \quad f_\psi|_{r=1} = \sigma_f, \quad f_\psi|_{z=\pm\frac{h}{2}} = -\frac{1}{r}\partial_r(\omega_\pm r^2) \tag{1.6a}$$

$$\Delta_h\psi = f_\psi, \quad \partial_r\psi|_{r=1} = 0, \quad \psi|_{r=0} = 0 \tag{1.6b}$$

$$(\partial_t - Re^{-1}\Delta)g = S_\phi, \quad g|_{r=1} = \sigma_g, \quad g|_{z=\pm\frac{h}{2}} = \sigma_g^\pm \tag{1.6c}$$

$$\Delta f_\phi = g, \quad f_\phi|_{r=1} = 0, \quad f_\phi|_{z=\pm\frac{h}{2}} = 0 \tag{1.6d}$$

$$\Delta_h\phi = f_\phi, \quad \phi|_{r=1} = 0 \tag{1.6e}$$

for the two potentials ψ, ϕ and three intermediate fields g, f_ψ and f_ϕ. The influence matrix technique [21], a generalization of the usual separation into particular and homogeneous solutions, is used to determine boundary values σ_f, σ_g, $\sigma_g^\pm$ such that the boundary conditions present in (1.5) but not in (1.6) are satisfied, i.e. such that

$$\partial_{rz}f_\psi - \frac{1}{r}\partial_\theta g = 0 \quad \text{at } r = 1 \tag{1.7a}$$

$$\frac{1}{r}\partial_\theta\psi + \partial_{rz}\phi = 0 \quad \text{at } r = 1 \tag{1.7b}$$

$$\partial_z f_\phi = 0 \quad \text{at } z = \pm\frac{h}{2} \tag{1.7c}$$

In this article, we describe the numerical implementation of this algorithm. We first present the spatial discretization of the fields, using a set of basis functions [22] which is regular at the cylindrical axis $r = 0$, and regularizing the discontinuous boundary conditions at the corners $r = 1$, $z = \pm h/2$. We then explain the methods we have used for solving Eq. (1.6), in particular for stably and economically solving the Helmholtz problems resulting from time discretization and for evaluating the nonlinear terms. Finally, we describe the validation of the implementation, comparing results from our code to an analytic polynomial solution and to previously published two- and three-dimensional test cases.

2. Spatial and temporal discretization

The spectral discretization that we use is

$$f(r,\theta,z) = \sum_{m=-\left\lfloor\frac{M}{2}\right\rfloor}^{\left\lfloor\frac{M}{2}\right\rfloor} f^m(r,z)e^{im\theta} = \sum_{m=-\left\lfloor\frac{M}{2}\right\rfloor}^{\left\lfloor\frac{M}{2}\right\rfloor}\sum_{k=0}^{K-1}\sum_{\substack{n=|m|\\ n+m\,\text{even}}}^{2N-1} f_{kn}^m e^{im\theta}\mathcal{Q}_n^m(r)\mathcal{T}_k\left(\frac{2z}{h}\right) \tag{2.1}$$

In (2.1), we do not introduce new notation for Fourier coefficients, or for coefficients in the 3D tensor-product basis, using instead the number and type of superscripts and subscripts to distinguish between functions in physical space and spectral space coefficients.

The basis functions in the azimuthal and axial directions are standard [23,24]: Fourier modes $e^{im\theta}$ and Chebyshev polynomials $\mathcal{T}_k(2z/h)$, respectively. In cylindrical geometries, it is the radial direction which is most problematic and on which we will focus. To represent this direction, we use the basis functions $\mathcal{Q}_n^m(r)$ developed by Matsushima and Marcus [22]. In Sections 2.1 and 2.2, we will discuss the means by which we impose regularity at the origin $r = 0$ and at the corners $r = 1$.

2.1. Regular basis of radial polynomials

A function f on the disk is analytic at the origin if the radial dependence of the Fourier coefficient $f^m(r)$ multiplying the Fourier mode $e^{im\theta}$ is of the form

$$f^m(r,z) = \sum_{\substack{n=|m| \\ n+m \text{ even}}}^{\infty} \alpha_n^m(z) r^m = \alpha_m^m(z) r^m + \alpha_{m+2}^m(z) r^{m+2} + \cdots = r^m p(r^2) \tag{2.2}$$

where p is a polynomial. Examples of functions which violate (2.2) are given in Figs. 1–3 and compared with regular functions obeying (2.2) on the right of each figure.

Various approaches used in spectral methods to represent functions in polar coordinates are surveyed by Boyd [25,26] and by Canuto et al. [24]. A common practice [8,14,21,27,28] has been to impose some degree of continuity, such as C^3, but not complete analyticity C^∞. Although basis functions which are not analytic at the origin generally do not pollute the fields, retaining such functions wastes CPU time and memory which could be better used to increase resolution.

The condition (2.2) is stated in terms of monomials, the use of which is excluded because of their poor numerical properties. The polynomial basis developed by Matsushima and Marcus [22] respects these conditions and yet is numerically well-conditioned. These polynomials $\mathcal{Q}_n^m(\alpha,\beta;r)$ are solutions to the singular Sturm–Liouville equation:

$$\left(\frac{(1-r^2)^{1-\alpha}}{r^\beta}\frac{\mathrm{d}}{\mathrm{d}r}\left((1-r^2)^\alpha r^\beta \frac{\mathrm{d}}{\mathrm{d}r}\right) - \frac{|m|(|m|+\beta-1)}{r^2} + n(n+2\alpha+\beta-1)\right)\mathcal{Q}_n^m(\alpha,\beta;r) = 0 \tag{2.3}$$

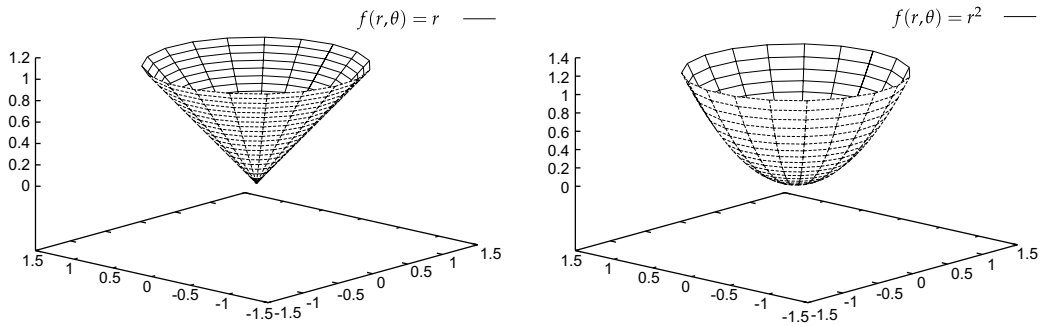

Fig. 1. Coordinate singularity effects: parity mismatch. Left: $f(r,\theta) = r$. Right: $f(r,\theta) = r^2$.

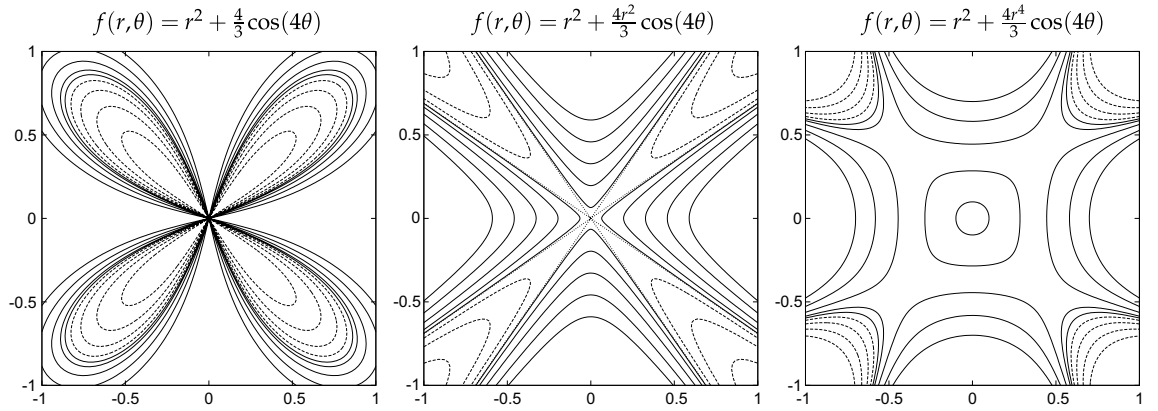

Fig. 2. Coordinate singularity effects. Left: discontinuity of value. Middle: discontinuity of Laplacian. Right: regular function.

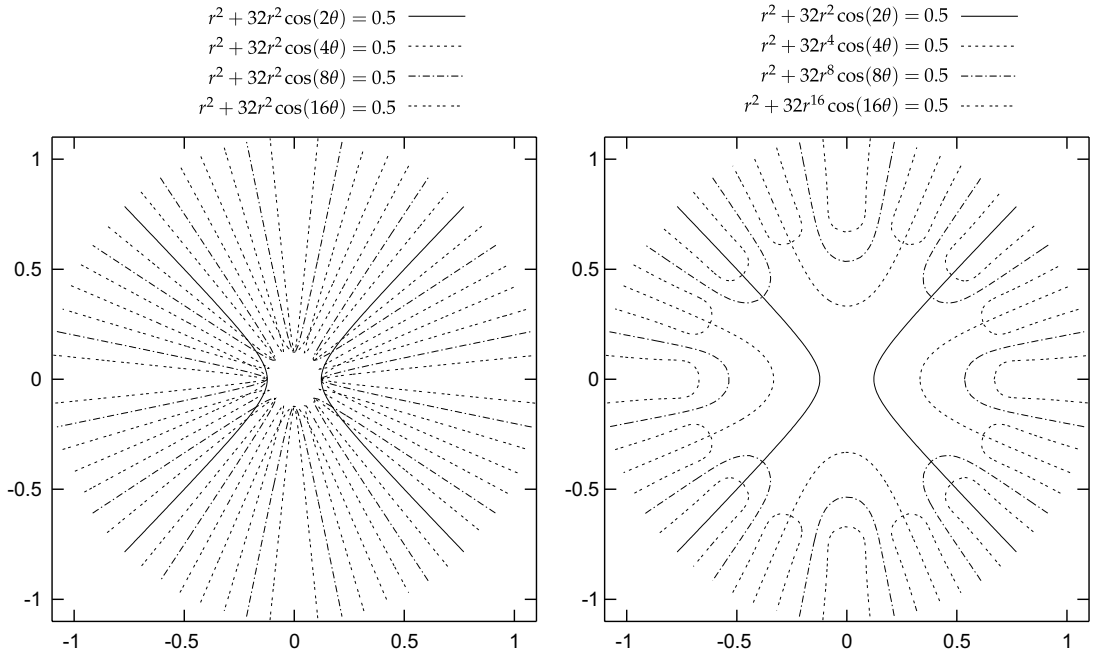

Fig. 3. Clustering effect – contours of $f^m(r,\theta) = 0.5$. Left: $f^m(r,\theta) = r^2 + 32r^2\cos(m\theta)$, which is not smooth at 0 for $m > 2$. Right: $f^m(r,\theta) = r^2 + 32r^m\cos(m\theta)$, which is smooth at 0.

defined over $r \in [0,1]$. In (2.3), $0 \leqslant |m| \leqslant n$, $\alpha \in [0,1]$ and β is a positive integer. With the special choice $\alpha = \beta = 1$, $\mathcal{Q}_n^m(1,1;r)$ are related to Legendre and shifted Jacobi polynomials used by Leonard and Wray [29]; similar functions were also derived by Verkley [30]. The functions $\mathcal{Q}_n^m(\alpha,\beta;r)$ are complete and orthogonal over $[0,1]$ with respect to the inner product:

$$\int_0^1 \mathcal{Q}_n^m(\alpha,\beta;r)\,\mathcal{Q}_{n'}^m(\alpha,\beta;r)\,\frac{r^\beta}{(1-r^2)^{1-\alpha}} = I_n^m(\alpha,\beta)\delta_{nn'} \tag{2.4}$$

The nth order polynomials $\mathcal{Q}_n^m(\alpha,\beta;r)$ have the following explicit expression:

$$\mathcal{Q}_n^m(\alpha,\beta;r) \equiv \sum_{p=0}^{\frac{n-|m|}{2}} \frac{(-1)^{p+\frac{n-|m|}{2}}\Gamma\left(\frac{n+|m|+\gamma-1}{2}+p\right)\Gamma\left(\frac{2|m|+\beta+1}{2}\right)}{\Gamma(p+1)\Gamma\left(\frac{n-|m|}{2}-p+1\right)\Gamma\left(\frac{2|m|+\beta+1}{2}+p\right)\Gamma\left(\frac{2|m|+\gamma-1}{2}\right)} r^{|m|+2p} \tag{2.5}$$

but they, as well as the normalizing coefficients $I_n^m(\alpha,\beta)$, can be calculated in $O(n-|m|)$ operations using recursion relations given by Matsushima and Marcus [22]. Recursion relations also exist for the operators

$$\{r\partial_r, r^2, (r\partial_r)^2 - m^2, (r\partial_r)^2 + \lambda r^2\} \tag{2.6}$$

expressed in the $\mathcal{Q}_n^m$ polynomial basis, meaning that for any of the operators H in (2.6), there exist banded matrices L and R such that $H = R^{-1}L$. Thus,

$$Hf = g \Longleftrightarrow Lf = Rg \tag{2.7}$$

reducing the time for multiplication by H or H^{-1} from quadratic to linear in the number of radial modes or gridpoints. The existence of recursion relations is a general property of differential operators represented in polynomial bases, for reasons explained by Tuckerman [31]. Recursion relations will be further discussed in Section 2.4.

The radial function $f^m(r)$ associated with Fourier mode m and its coefficients f_n^m in the polynomial basis are related by the transform pair:

$$f^m(r) = \sum_{\substack{n=|m| \\ n+m \text{ even}}}^{\infty} f_n^m \mathcal{Q}_n^m(r) \approx \sum_{\substack{n=|m| \\ n+m \text{ even}}}^{\widehat{N}} f_n^m \mathcal{Q}_n^m(r) \tag{2.8a}$$

$$f_n^m = \int_0^1 \mathrm{d}r w(r) f^m(r) \mathcal{Q}_n^m(r)/I_n^m \approx \sum_{i=0}^{N-1} w_i f^m(r_i) \mathcal{Q}_n^m(r_i)/I_n^m \tag{2.8b}$$

In (2.8), the order of the polynomial expression is $\widehat{N} \equiv 2N-2$ or $\widehat{N} \equiv 2N-1$ according to whether m is even or odd. The collocation points $\{r_i\}$ for Gaussian quadrature are computed numerically as the roots of the first neglected $m=0$ polynomial $\mathcal{Q}^0_{\widehat{N}+2}$ if the boundary points are to be excluded; otherwise, they are the roots of a slightly more complicated expression [22]. Once the $\{r_i\}$ are determined, the weights $\{w_i\}$ are computed by recursion relations [22].

Eq. (2.8) specify $N_m \equiv N - [m/2]$ coefficients from values at N quadrature points via a rectangular matrix. Since the basis is orthonormal, the inverse transformation is obtained from the transpose of this rectangular matrix. The smaller size of the spectral representation compared to the grid representation is a consequence of the fact that the functions in (2.8) are not arbitrary functions of r, but belong to the restricted subspace of functions obeying the regularity conditions (2.2).

2.2. Regularization of the corners

The boundary conditions on u_θ stated in (1.2) are

$$u_\theta(r,\theta) = r\omega_\pm \quad \text{at } z = \pm\frac{h}{2} \tag{2.9a}$$

$$u_\theta(\theta,z) = 0 \qquad \text{at } r = 1 \tag{2.9b}$$

The equations have been non-dimensionalized using the radius as the unit of length and the inverse angular velocity $1/\omega_-$ (with $\omega_- > 0$ and $|\omega_+| \leqslant \omega_-$) as the unit of time. Therefore, $\omega_- = 1$ and $-1 \leqslant s = \omega_+ \leqslant 1$, in particular ω_+ is 0, +1 or −1, for the rotor–stator, exactly corotating, or exactly counter-rotating configurations, respectively. (It is also possible to set the velocity on the cylinder to some other constant value instead of 0; for example to simulate the flow in a rotating cylinder, we would set $u_\theta|_{r=1}(\theta, z) = \omega_+ = \omega_- = 1$.) Here, we focus instead on the difficulties in implementing the discontinuous boundary conditions (2.9).)

Boundary conditions (2.9) are discontinuous at the corner points $r=1$, $z=-h/2$ and possibly $r=1$, $z=+h/2$: one or both disks rotate while the lateral boundary remains fixed. Mathematically, a PDE with a finite number of singular points can have a solution which is smooth except at these points. However, spectral methods then do not converge exponentially because series of smooth functions cannot converge uniformly to a discontinuous solution. If nothing is done to prevent it, the Gibbs phenomenon will lead to spurious oscillations which propagate into the whole domain from the neighborhood of the singularity. For finite difference methods, the discontinuity will affect only the neighborhood of the singular point, on the order of the grid interval, and therefore does not pose a severe problem. Finite volume methods have a local integral formulation and so the discontinuity presents an even less serious problem. The filtering intrinsic to local methods is, however, intrinsically related to the high numerical diffusion which in turn makes local methods less precise. In some cases, even local methods do not sufficiently filter singularities. Georgiou et al. [32] discuss the issue of spurious oscillations in the context of finite element methods. In the solutocapillary problem studied by Martin-Witkowski and Walker [33], the authors were required to explicitly filter the solution to achieve acceptable convergence even in a finite difference calculation.

Spectral methods must always explicitly filter strong singularities like (2.9a) and (2.9b). We have chosen to do this by approximating the discontinuous function at the boundary by a steep but smooth profile. This procedure can be justified by arguing that we are not interested in finding the solution to the singular problem. In any real experiment, the boundary conditions are not discontinuous: a small gap must necessarily exist between the rotating disks and the stationary lateral boundary. In our algorithm, we replace the constant angular velocities in (2.9a) by continuous functions, as illustrated by Fig. 4a. Two possibilities are:

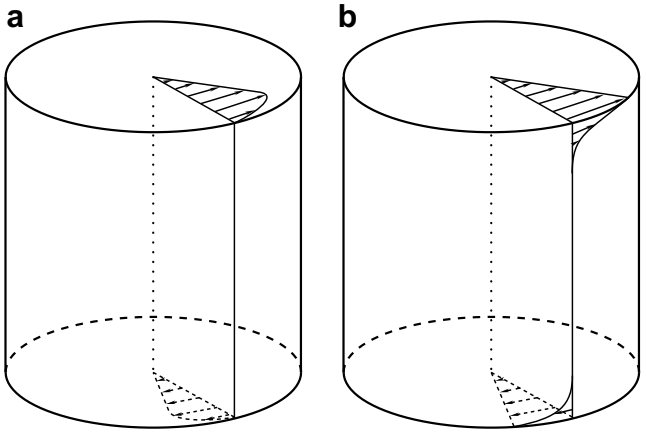

Fig. 4. Regularized profiles used for elimination of the discontinuous boundary conditions at the cylinder corners. (a) regularization on upper and bottom disks using (2.10). (b) regularization on lateral bounding cylinder using (2.11).

$$u_\theta(r,\theta) = r\left(1 - \mathrm{e}^{\frac{r-1}{\delta}}\right)\omega_\pm \quad \text{at } z = \pm\frac{h}{2} \tag{2.10a}$$

$$u_\theta(r,\theta) = r(1 - r^\mu)\omega_\pm \quad \text{at } z = \pm\frac{h}{2} \tag{2.10b}$$

where μ is an arbitrary but large even integer (e.g. $\mu = 10$), and δ, $\omega_\pm$ are constants. In order to be represented in a radial polynomial basis, the exponential regularization (2.10a) must be approximated by a polynomial, so that both expressions above are effectively polynomials. The steepness of the profiles are adjusted by varying δ or μ, whose possible values are limited by the radial polynomial order N.

The advantage of exponential regularization is that, for a given N, a steeper profile can be achieved by the polynomial approximation to (2.10a) than by the polynomial (2.10b), as can be seen in Fig. 5(a). In this way, the deviation from the idealized profile is minimized, without unduly increasing the radial resolution N over that required to resolve the field in the interior. The polynomial approximation to (2.10a) differs from 1 by more than 10% only over the small range $1 - 2\delta \lesssim r < 1$.

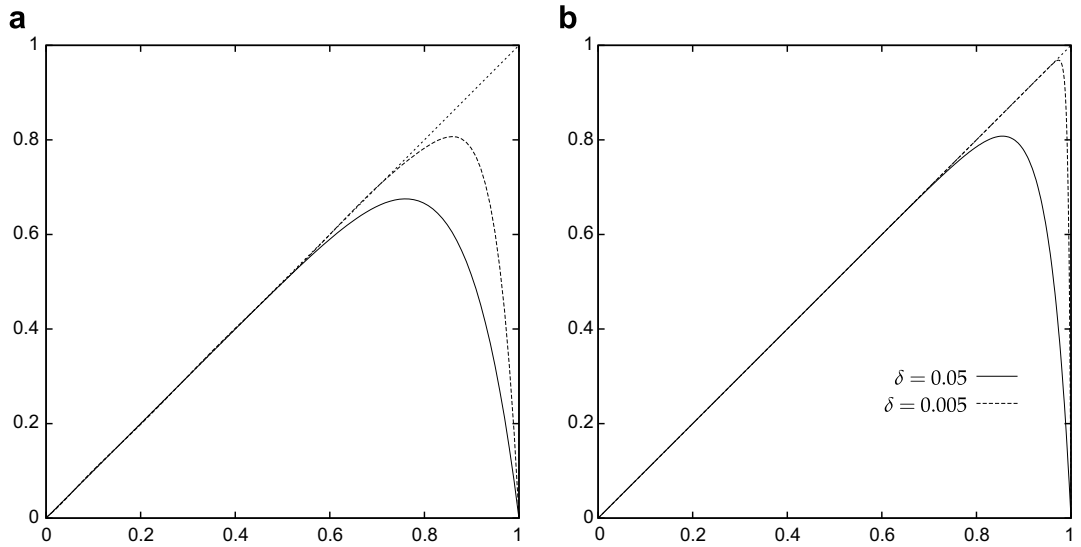

Fig. 5. (a) Comparison between regular profiles represented by polynomials of order r^9. Solid curve: $u_\theta|_{z=\pm\frac{h}{2}}(r) = r(1 - r^8)$. Dotted curve: $u_\theta|_{z=\pm\frac{h}{2}}(r) \approx r(1 - \mathrm{e}^{\frac{r-1}{\delta}})$. Inset illustrates result (b) Comparison between exponential profiles $u_\theta|_{z=\pm\frac{h}{2}}(r) = r(1 - \mathrm{e}^{\frac{r-1}{\delta}})$ for different δ.

Regularization of the boundary condition imposes a lower bound on the spectral resolution – the spectral approximation must be able to represent the regularization profiles smoothly. In fact, Lopez and Shen [7] observed that the actual resolution should be approximately twice the minimal resolution sufficient for representing the regularization profiles, due to generation of higher wavenumbers by the nonlinear terms. As was shown by Lopez and Shen [7], for comparing with results obtained using different methods and for benchmark purposes it is sufficient to use $\delta \approx 0.005$. In practice, we use $0.005 < \delta < 0.05$, illustrated in Fig. 5(b).

Care must be taken in approximating (2.10a) by a polynomial expression, in order to satisfy all of the conditions in (1.5a)–(1.5b) that we require of u_θ and of ψ. The procedure we use is as follows. We evaluate (2.10a) on the collocation points. Since u_θ is an odd function of r (see (2.29)), we apply the transform (2.8) using the (odd) polynomials associated with the $m = 1$ Fourier mode. The basis of odd radial functions insures that this approximation to u_θ on the bounding disks is zero at $r = 0$, while the use of Gauss–Radau collocation points which include the cylinder boundary insures that it is also zero at $r = 1$. This approximation to u_θ is integrated over r to obtain an approximation to ψ, with the integration constant chosen in order to satisfy $\psi = 0$ at $r = 0$.

Another choice is to apply a filter to the lateral boundary, replacing (2.9b) by

$$u_\theta(z) = \omega_+ e^{-\left(1-\frac{2z}{h}\right)/\delta} + \omega_- e^{-\left(1+\frac{2z}{h}\right)/\delta} \quad \text{at } r = 1 \tag{2.11}$$

while keeping the uniform angular velocity profiles (2.9a) on the disks unchanged; see Fig. 4(b). This kind of regularization is similar to that of Lopez and Shen [7].

Other, quite different, approaches to the treatment of singularities exist. One is singularity subtraction. The form of the singular part of the solution is determined analytically, and the solution is written as a sum of the singular solution and an unknown regular part. Only the regular part is treated numerically. The effect of the singular solution on the numerical one can be filtered down to the scales representable by the spatial resolution. The main advantage of this method is that it recovers the convergence of the scheme and at the same time approaches the exact solution. Recent applications of this method are to the driven cavity problem [34] and to injection of fluid into a cylindrical channel [35]. The results obtained are generally of high precision and often provide a benchmark for a particular problem. The main drawback is that it requires knowledge of the solution near the singular point. For the 2D driven cavity problem, the nature of the singularity was given by Dean and Montagnon [36] and Moffatt [37] for a Stokes flow. For most inertial (Navier–Stokes) flows, and for 3D flows, as shown by Hills and Moffatt [38], the analytic form of the singular solution is unknown. Note that even when the velocity boundary conditions are continuous, lower-order singularities of purely geometric origin are present at the corners. We will return to this in Section 3.2.

Another approach is to derive a physically justified model which is no longer singular. Methods from molecular dynamics reflect the microscopic nature of the fluid at the smallest scales but are very hard to adapt to problems containing both large and small scales. Several continuous (macroscopic) approaches have been proposed as a compromise between a continuous and a molecular description. These all introduce a spatially limited physical effect which effectively removes the singularity. In this category are methods based on variable slippage, as well as the surface viscosity or dynamic surface tension applicable to free-surface problems. A comprehensive review of physically justified models, as well as other regularization techniques, is provided by Nguyen and co-workers [39,40].

2.3. Time integration

We use an implicit scheme for the linear diffusive terms while treating the nonlinear terms explicitly. Spectral methods require that the coefficients representing the solution decay with their index or wavenumber. The nonlinear term in the Navier–Stokes equation can be seen as a generator and amplifier of high wavenumbers while the viscous term damps these high wavenumbers. The intensity of this damping depends on the particular time-integration scheme and on the way the Laplacian is evaluated and must be strong enough to oppose the effect of the nonlinear term. In our case, high-wavenumber modes are needed to represent both the thin boundary layers created near the rotating disks and the steep regularized boundary profile. Fortunately, these effects are most pronounced in the proximity of the boundaries, where the axial Chebyshev and radial polynomial grid is finest. However, in the counter-rotating case, the central shear layer can also require high wavenumber modes in order to be well-represented.

We use the first-order backward Euler scheme for linear terms because it attenuates high wavenumbers faster than all other methods. Tests performed with the Crank–Nicolson method confirmed that for this scheme, nonlinear simulation was unstable even for quite small Reynolds numbers $Re \approx 300$. This behavior was also observed for the von Kármán flow by Lopez et al. [14] and Speetjens [41] and by Marcus [42] for Taylor–Couette flow.

When the nonlinear term is treated by the second-order explicit Adams–Bashforth scheme, the backward Euler/Adams–Bashforth time-integration scheme for the potentials ψ and ϕ takes the following form:

$$(I - \delta t Re^{-1}\Delta)\Delta_h \psi^{n+1} = \Delta_h \psi^n + \frac{\Delta t}{2}\left(3S_\psi^n - S_\psi^{n-1}\right) \equiv \mathrm{rhs}_\psi^n \tag{2.12a}$$

$$(I - \delta t Re^{-1}\Delta)\Delta\Delta_h \phi^{n+1} = \Delta\Delta_h \phi^n + \frac{\Delta t}{2}\left(3S_\phi^n - S_\phi^{n-1}\right) \equiv \mathrm{rhs}_\phi^n \tag{2.12b}$$

where S_ψ and S_ψ are defined in (1.4). Our algorithm could easily be adapted to integrate the diffusive terms via the backwards differentiation scheme, which achieves second-order accuracy while damping high wavenumbers, merely by changing the coefficients in (2.12) and including terms in ψ^{n-1} and ϕ^{n-1}.

Eq. (2.12) can be written as the nested system of equations:

$$\left(I - \delta t Re^{-1}\Delta\right) f_\psi = \mathrm{rhs}_\psi \tag{2.13a}$$

$$\Delta_h \psi = f_\psi \tag{2.13b}$$

$$\left(I - \delta t Re^{-1}\Delta\right) g = \mathrm{rhs}_\phi \tag{2.13c}$$

$$\Delta f_\phi = g \tag{2.13d}$$

$$\Delta_h \phi = f_\phi \tag{2.13e}$$

As explained in Section 1, the boundary conditions imposed on (2.13) are Dirichlet conditions with boundary values calculated via the influence matrix in such a way as to satisfy the more complicated coupled boundary conditions given in (1.5).

The maximal time step δt depends on the Reynolds number. Typically starting from state $\mathbf{u} = 0$ requires a δt which is 4–10 times smaller than that which can be used for evolving a fully developed state at the same Reynolds number. This is because the state $\mathbf{u} = 0$ is incompatible with the boundary condition (2.9a). In the first few iterations a boundary layer is created near the rotating cylinder lids, requiring higher spatial resolution. This can be avoided by performing about 100 initial steps of the linear Stokes solver, i.e. with $S_\psi = S_\phi = 0$.

In Table 1 we present the values of δt and spatial resolutions typically used for performing nonlinear simulations at different values of Re.

2.4. Viscous terms

We now describe the way in which the Helmholtz and Poisson problems with Dirichlet boundary conditions in (1.6) or (2.13) are solved. The azimuthal Fourier representation in (2.1) decomposes each 3D elliptic

Table 1
Typical values of timestep δt and azimuthal (M), axial (K) and radial (N) resolution, for different configurations

Re	Configuration	δt	Resolution ($M \times K \times N$)
<O(500)	2D	0.05–0.1	$1 \times 32 \times 16$
500–1000	2D	0.02–0.05	$1 \times 64 \times 32$
1000–3000	2D	0.01–0.02	$1 \times 96 \times 48$
3000–5000	2D	0.005–0.01	$1 \times 128 \times 64$
5000–10,000	2D	0.001–0.0025	$1 \times 180 \times 90$
<O(500)	3D	0.04–0.1	$8 \times 64 \times 32$
500–1000	3D	0.01–0.04	$16 \times 80 \times 40$
1000–3000	3D	0.025–0.01	$32 \times 100 \times 60$
3000–5000	3D	0.001–0.0025	$(64–96) \times 128 \times 80$

Typical steepness of the regularization profile is $\delta \approx 0.01$.

problem into a set of 2D problems, each of which is associated to a single azimuthal Fourier mode m. The reflection symmetry in z leads to further decoupling between the set of modes that are symmetric or antisymmetric in z. Each of the $2M$ resulting elliptic problems corresponds to a single azimuthal Fourier mode m and axial parity $p \in \{s,a\}$, within which each equation corresponds to a value of (k,n), the indices of the axial and radial basis functions. The number of axial modes of each parity is $K/2$, and the number of radial basis functions corresponding to Fourier mode m is $N_m \equiv N - [\frac{m}{2}]$; in the remainder of this section, we will take $m = 0$, so that $N_m = N$.

In the full cylinder, regularity at the axis serves as one of the boundary conditions and is imposed by the use of the $\mathcal{Q}_n$ radial basis in (2.1), leaving only the boundary condition at $r = 1$ to be imposed. In the axial direction, the boundary conditions at the two disks can be recombined to yield one condition for each parity. Thus, one radial and one axial boundary condition remains to be imposed on each 2D problem. These are imposed via the τ method [23,24], so that the equations corresponding to the highest-wavenumber modes in each direction are replaced by the boundary conditions.

Gaussian elimination is especially economical for systems resulting from the spectral discretization of differential equations, whose structure is barely altered when boundary conditions are imposed via the τ method, since recursion relations reduce the solution time from quadratic to linear in the number of modes if the resulting systems are diagonally dominant. This can only be done in one direction however. In geometries with more than one non-periodic direction, the remaining directions must be treated by diagonalization. Here, we treat the axial direction by incorporating the boundary condition via Schur decomposition into the matrices representing ∂_z^2 for each parity and diagonalizing [24,43], leading to decoupled problems for each axial eigenvalue λ_z. The operation count at each timestep, dominated by multiplication by the eigenvector matrix, is quadratic in $K/2$ and linear in N.

Thus, the 2D and 3D problems in (2.13) are all decomposed into a set of one-dimensional radial problems:

$$Hf \equiv \left[\frac{1}{r}\partial_r r \partial_r - \frac{m^2}{r^2} + \lambda\right] f = g \tag{2.14}$$

which we will write in practice as

$$r^2 Hf \equiv \left[r\partial_r r\partial_r - m^2 + \lambda r^2\right] f = r^2 g \tag{2.15}$$

where m is the Fourier mode. The scalar λ is 0 or λ_z for the Poisson problems (2.13b), (2.13d) or (2.13e), or $\lambda_z + Re/\delta t$ for the Helmholtz problems (2.13a) and (2.13c) (with the multiplicative factor $-Re/\delta t$ incorporated into g).

With f and g represented in the polynomial radial basis (2.8), a recursion relation exists for $r^2 H$, as stated in Section 2.1, i.e. $r^2 H = R^{-1} L$ with R, L banded matrices. Thus each Helmholtz problem (2.15) can be replaced by

$$Lf = Rr^2 g \equiv Qg \tag{2.16}$$

For non-zero λ, L is pentadiagonal and R is tridiagonal. Two obstacles must still be surmounted before (2.16) can be solved in a time which is linear in the number of radial modes. A method which overcomes them was presented by Matsushima and Marcus [22]. Here, we will recast this method in terms of the Sherman–Morrison–Woodbury formula, which can be shown [21] to underly a large class of transformations between coupled and uncoupled systems.

The first obstacle is that L is not diagonally dominant, so that stable Gaussian elimination would require pivoting, destroying the banded structure. Since the largest element of L is located on the first super-diagonal, permuting its rows leads to a matrix PL which is diagonally dominant, but is no longer banded.

Second, the radial boundary condition must be imposed. The tau method replaces (2.15) by

$$Hf = g + \hat{e}_N \tau \tag{2.17a}$$

$$B^{\mathrm{T}} f = \beta \tag{2.17b}$$

which effectively discards g_N by adjusting it with the extra unknown τ, introduced along with the boundary condition (2.17b). B^{T} is the row vector which represents the discretized boundary condition and $\hat{e}_N$ is the unit vector which selects the Nth component. Multiplying (2.17a) by r^2, substituting the banded matrix decomposition (2.16) and permuting rows leads to:

$$\begin{aligned} r^2 Hf &= R^{-1} Lf = r^2 g + r^2 \hat{e}_N \tau \\ Lf &= Rr^2 g + Rr^2 \hat{e}_N \tau \\ PLf &= PQg + PQ\hat{e}_N \tau \end{aligned} \tag{2.18}$$

Eqs. (2.18) and (2.17b) are rewritten in matrix form as

$$\left(\begin{array}{c|c} L_{N,i} & -Q_{N,N} \\ \hline L_{lo,i} & -Q_{lo,N} \\ \hline B^T & 0 \end{array}\right) \left(\begin{array}{c} f \\ \hline \tau \end{array}\right) = \left(\begin{array}{c} (Qg)_N \\ \hline (Qg)_{lo} \\ \hline \beta \end{array}\right) \tag{2.19}$$

where the subscript *lo* refers to all indices lower than N. System (2.19) is solved by using the Sherman–Morrison–Woodbury formula

$$(A + vw^{\mathrm{T}})^{-1} = A^{-1} - A^{-1} v (I + w^{\mathrm{T}} A^{-1} v)^{-1} w^{\mathrm{T}} A^{-1} \tag{2.20}$$

which relates the inverses of two matrices differing by a low-rank transformation vw^{T}, in particular differing by a few rows or columns. We define A, v and w^{T} for (2.19) as follows. The coupled matrix in (2.19), which corresponds to $(A + vw^{\mathrm{T}})$, is replaced by another matrix A, which is more easily inverted since it is block upper triangular:

$$A \equiv \left(\begin{array}{c|c} a\hat{e}_1^T & -Q_{N,N} \\ \hline L_{lo,i} & -Q_{lo,N} \\ \hline 0 & 1 \end{array}\right) \equiv \left(\begin{array}{c|c} L' & -q \\ \hline 0 & 1 \end{array}\right) \tag{2.21}$$

where a is an arbitrary value whose order of magnitude is that of the dominant values of L and $\hat{e}_1^{\mathrm{T}}$ is a unit row vector corresponding to the lowest radial wavenumber present for this m. The crucial property of the matrix L' defined in (2.21) is that it is both banded and diagonally dominant and so can be stably inverted without any pivoting. The matrices in (2.21) and (2.19) differ only in their first and last rows, so their difference vw^{T} is of rank two:

$$\left(\begin{array}{c|c} \hat{e}_N L - a\hat{e}_1^T & 0 \\ \hline 0 & 0 \\ \hline B^T & -1 \end{array}\right) = \left(\begin{array}{c} 1\ 0 \\ \hline 0\ 0 \\ \hline 0\ 1 \end{array}\right) \left(\begin{array}{cc|c} \hat{e}_N - a\hat{e}_1^T & & 0 \\ & B^T & -1 \end{array}\right) \equiv vw^T \tag{2.22}$$

In addition to the ability to solve (2.21), the Sherman–Morrison–Woodbury formula (2.20) requires only the inversion of the following 2×2 matrix:

$$\begin{aligned} I + w^T A^{-1} v &= I + \left(\begin{array}{cc|c} \hat{e}_N^T L - a\hat{e}_1^T & & 0 \\ & B^T & -1 \end{array}\right) \left(\begin{array}{c|c} (L')^{-1} & (L')^{-1} q \\ \hline 0 & 1 \end{array}\right) \left(\begin{array}{c} 1\ 0 \\ \hline 0\ 0 \\ \hline 0\ 1 \end{array}\right) \\ &= \begin{pmatrix} \hat{e}_N^T L (L')^{-1} \hat{e}_1 & (\hat{e}_N^T L - a\hat{e}_1^T)(L')^{-1} q \\ B^T (L')^{-1} \hat{e}_1 & B^T (L')^{-1} q \end{pmatrix} \end{aligned} \tag{2.23}$$

where we have used the fact that $a\hat{e}_1^{\mathrm{T}} (L')^{-1} \hat{e}_1 = 1/a$. The notation $(L')^{-1}$ is used to designate solving a linear system involving L' via backsolving rather than explicitly calculating the inverse matrix.

2.5. Nonlinear terms

To compute the nonlinear terms

$$S_\psi \equiv \hat{\mathbf{e}}_z \cdot \nabla \times \mathbf{S} \tag{2.24a}$$

$$S_\phi \equiv -\hat{\mathbf{e}}_z \cdot \nabla \times \nabla \times \mathbf{S} \tag{2.24b}$$

where

$$\mathbf{S} \equiv (\mathbf{u}\cdot\nabla)\mathbf{u} = \frac{1}{2}\nabla(\mathbf{u}\cdot\mathbf{u}) - \mathbf{u}\times\boldsymbol{\omega} \tag{2.25}$$

we use the pseudo-spectral method [23], in which fields are transformed into physical space, the nonlinear terms are carried out via pointwise multiplication, and the results transformed back into spectral space. Computing the nonlinear term $\mathbf{S}$ in the rotational form $-\mathbf{u}\times\boldsymbol{\omega}$ requires only 9 spectral $\leftrightarrow$ physical transforms as compared to the 15 transforms required by the convective form $(\mathbf{u}\cdot\nabla)\mathbf{u}$. The difference between them is annihilated by the curls taken in (2.24), so we will write $\mathbf{S} = -\mathbf{u}\times\boldsymbol{\omega}$.

The calculation of the nonlinear terms presents two difficulties. The first involves radial parity and appears when creating $\mathbf{S}$. We have sought to use only scalar fields which can be represented by expansions of type (2.1). Such fields can be constructed using radial operators such as (2.6) which preserve radial parity and can be implemented via recursion relations. The components of velocity and vorticity, defined in cylindrical coordinates using the toroidal and poroidal potentials as

$$\mathbf{u} = \left(\frac{1}{r}\partial_\theta\psi + \partial_{rz}\phi\right)\hat{\mathbf{e}}_r + \left(\frac{1}{r}\partial_{\theta z}\phi - \partial_r\psi\right)\hat{\mathbf{e}}_\theta + (\Delta_h\phi)\hat{\mathbf{e}}_z \tag{2.26a}$$

$$\boldsymbol{\omega} = \left(\partial_{rz}\psi - \frac{1}{r}\partial_\theta\Delta\phi\right)\hat{\mathbf{e}}_r + \left(\frac{1}{r}\partial_{\theta z}\psi - \partial_r\Delta\phi\right)\hat{\mathbf{e}}_\theta + \frac{1}{r}(-\Delta_h\psi)\hat{\mathbf{e}}_z \tag{2.26b}$$

do not have this property. We therefore construct modified fields:

$$\mathbf{u}^* \equiv ru_r\hat{\mathbf{e}}_r + ru_\theta\hat{\mathbf{e}}_\theta + u_z\hat{\mathbf{e}}_z = (\partial_\theta\psi + r\partial_{rz}\phi)\hat{\mathbf{e}}_r + (\partial_{\theta z}\phi - r\partial_r\psi)\hat{\mathbf{e}}_\theta + (\Delta_h\phi)\hat{\mathbf{e}}_z \tag{2.27a}$$

$$\boldsymbol{\omega}^* \equiv r\omega_r\hat{\mathbf{e}}_r + r\omega_\theta\hat{\mathbf{e}}_\theta + \omega_z\hat{\mathbf{e}}_z = (\partial_\theta u_z - \partial_z u_\theta^*)\hat{\mathbf{e}}_r + (\partial_z u_r^* - r\partial_r u_z)\hat{\mathbf{e}}_\theta + (-\Delta_h\psi)\hat{\mathbf{e}}_z \tag{2.27b}$$

whose components have the same parity as ψ and ϕ, as desired. The modified fields $\mathbf{u}^*$ and $\boldsymbol{\omega}^*$ are transformed into physical space, where their cross product is taken to form

$$\mathbf{S}^* \equiv rS_r\hat{\mathbf{e}}_r + rS_\theta\hat{\mathbf{e}}_\theta + S_z\hat{\mathbf{e}}_z \equiv S_r^*\hat{\mathbf{e}}_r + S_\theta^*\hat{\mathbf{e}}_\theta + S_z^*\hat{\mathbf{e}}_z = -\mathbf{u}^*\times\boldsymbol{\omega}^* \tag{2.28}$$

The second difficulty appears when differentiating $\mathbf{S}$ in (2.24) and involves regularity. A vector function which is analytic at the origin must obey conditions analogous to (2.2), namely

$$f_r(r) = r^{|m-1|}p_r(r^2), \quad f_\theta(r) = r^{|m-1|}p_\theta(r^2), \quad f_z(r) = r^m p_z(r^2) \tag{2.29}$$

where p_r, p_θ and p_z are polynomials. We require not only regularity at the origin of $\mathbf{S}$, but also regularity of its curl and double curl. When $\mathbf{S} = -\mathbf{u}\times\boldsymbol{\omega}$ is calculated analytically, this is in fact the case. However, the numerical transforms to and from physical space introduce aliasing errors which destroy this property. Full dealiasing would multiply the time necessary for evaluating of the nonlinear term by a factor of about 4.5. Matsushima and Marcus [22] suggest instead that all terms that could potentially suffer in spectral space from singular operations (like dividing by r) be evaluated in physical space (at collocation points excluding the coordinate origin) and transformed back to the spectral space using the radial transform, ensuring the correct polynomial order for a given Fourier mode. We have generalized this approach to the evaluation of S_ψ and S_ϕ. For each Fourier mode m, we write

$$S_\psi = \frac{1}{r}(\partial_r rS_\theta - \mathrm{i}mS_r) = \frac{1}{r^2}(r\partial_r - m)S_\theta^* - \frac{\mathrm{i}m}{r^2}(S_r^* + \mathrm{i}S_\theta^*) \tag{2.30a}$$

$$S_\phi = -\frac{1}{r}\partial_z(\partial_r rS_r + \mathrm{i}mS_\theta) + \Delta_h S_z = -\frac{1}{r^2}\partial_z(r\partial_r - m)S_r^* + \Delta_h S_z - \frac{m}{r^2}\partial_z(S_r^* + \mathrm{i}S_\theta^*) \tag{2.30b}$$

Table 2
CPU timings on an IBM Power4, as a function of azimuthal resolution M and number of processors

	Number of processors	Resolution $M \times K \times N$	CPU (s)/timestep	CPU (s)/(timestep $\times M$)
2D	Single processor	$1 \times 96 \times 48$	0.035	0.035
3D	Single processor	$32 \times 96 \times 48$	1.7 s	0.053
3D	32 processors	$32 \times 96 \times 48$	1.5 s	0.047

The purpose of the decomposition in (2.30) can be explained as follows. Consider the first terms on the rightmost-sides of (2.30), those which do not contain $(S_r^* + \mathrm{i}S_\theta^*)$. Because they do not generate terms of lower polynomial order, these terms preserve regularity and can be carried out in spectral space. In contrast, although $(S_r^* + \mathrm{i}S_\theta^*)$ should be divisible by r^2, aliasing error in the multiplication (2.27) can generate terms of lower polynomial order. (More specifically, S_r^* and iS_θ^* are not individually divisible by r^2 and aliasing perturbs the cancellation in the sum $S_r^* + \mathrm{i}S_\theta^*$.) This division by r^2 is therefore carried out in physical space. This increases the number of spectral $\leftrightarrow$ physical transformations only from 9 to 10. Further details can be found in [44].

2.6. Parallelization

The separability of almost the entire algorithm (except for the nonlinear term) between the Fourier modes makes parallelization of the code quite straightforward. Our code was parallelized using the MPI protocol which made it possible to run even very time-consuming three-dimensional simulations with resolutions such as $M \times K \times N = 128 \times 160 \times 90$. Spectral methods are often considered to be poorly suited for parallelization as they require the exchange of all the data at each timestep of the simulation. In our code, all the necessary data exchange is done within two calls to the *MPI_Alltoall* MPI subroutine treating, in total, 10 three-dimensional fields at each time step. Even though this may seem to be a large operation, on the IBM Power4 architecture with 64 processors we found that the time overhead per timestep due to the data exchange is counterbalanced by more efficient usage of the processor cache memory: each processor of the parallelized code treats smaller data portions which can more easily fit into the processor's fast internal memory (cache). We observed that the total CPU time used by the parallel code is often smaller than that used by the serial code treating the same problem, as shown in Table 2. The efficiency of the parallel code depends, however, on the speed and the latency of the inter-processor network: the IBM Power4 architecture has particularly fast connection between the nodes which use the mixed model *fast network/shared memory* communication between processors. We conclude that for modern massively parallel computers, parallelization of a pseudo-spectral code does not necessarily degrade its efficiency but can actually enhance it. Additional technical information about the MPI parallelization of the code is given in [44].

3. Tests and validation

We now describe the ways in which we have validated the hydrodynamic code described here and in our companion paper [20]. We have obtained exact polynomial solutions to the nested Helmholtz–Poisson solver, which is by far the most complicated portion of the code; we present its form in the hopes it may prove useful to other researchers. For non-polynomial solutions, we have analyzed the effect of the corner singularity on the error and verified the spectral convergence. We have tested the full nonlinear time-dependent program by simulating 2D and 3D stationary and time-periodic rotor–stator flows which are well documented in the literature.

3.1. Polynomial solutions

No analytic solutions are available for the time-dependent nonlinear differential equations (1.4) and boundary conditions (1.5) with which to compare a numerical solution. We can, however, formulate polynomial solutions to the time-discretized equations

$$E\Delta_h\psi \equiv (I - \delta t Re^{-1}\Delta)\Delta_h\psi = \mathrm{rhs}_\psi \tag{3.1a}$$

$$E\Delta\Delta_h\phi \equiv (I - \delta t Re^{-1}\Delta)\Delta\Delta_h\phi = \mathrm{rhs}_\phi \tag{3.1b}$$

relating the four fields ψ, ϕ, rhs_ψ, rhs_ϕ. The fields ψ and ϕ are chosen to be regular polynomials obeying boundary conditions (1.5). The fields rhs_ψ and rhs_ϕ are then calculated analytically by acting with the differential operators E, Δ and Δ_h on ψ, ϕ as specified in (3.1). We also require that rhs_ψ and rhs_ϕ be expressible as the $\hat{\mathbf{e}}_z$ component of the curl and double curl of a vector field $\mathbf{S}$ as specified in (2.24). $\mathbf{S}$ must in turn be expressible as the vector product $-\mathbf{u}\times\boldsymbol{\omega}$ of two regular vector fields, as specified in (2.25). However, $\mathbf{u}$ and $\boldsymbol{\omega}$ are not required to be derived from the potentials ψ and ϕ, and so this construction does not lead to a solution to the Navier–Stokes equations. These requirements on rhs_ψ and rhs_ϕ restrict the possible forms of the polynomials ψ and ϕ.

When ψ and ϕ are constructed in this way, no error is introduced in imposing the boundary conditions via the τ method (see Section 2.4). Comparison between this analytic solution and a numerical solution provides a test of the linear Helmholtz/Poisson solver, including the enforcement of the boundary conditions via the influence matrix method.

Using a symbolic algorithm implemented in Maple, we have calculated polynomial solutions which contain several radial and axial basis functions (wavenumbers) and which correspond to a realistic profile $\omega_\pm$, such as $\omega_\pm^{\mathrm{poly}} = \pm(1-r^6)$. Polynomial solutions were calculated for Fourier modes ranging from $m=0$ to $m=5$. For $m=0$, we sought a solution containing two recirculation rolls separated by the mid-plane $z=0$, leading to the potentials, right-hand-sides and velocities:

$$\psi^{\mathrm{poly}}(r,z) = \frac{1}{64}z(-30z^2+33z^4+5)r^8 - \frac{5}{48}z(z-1)(z+1)(5z^2-1)r^6 - \frac{1}{2}z^5r^2 \tag{3.2a}$$

$$\mathrm{rhs}_\psi^{\mathrm{poly}}(r,z) = -z(-690z^2+33z^4+185)r^6 + \frac{3}{4}z(-1970z^2+425+1609z^4)r^4 - 60z(z-1)(z+1)(5z^2-1)r^2 - 40z^3+2z^5 \tag{3.2b}$$

$$\phi^{\mathrm{poly}}(r,z) = -\frac{1}{2}(r-1)^3(r+1)^3(z-1)^2(z+1)^2z \tag{3.2c}$$

$$\mathrm{rhs}_\phi^{\mathrm{poly}}(r,z) = -72z(5z^2-33)r^4 - 96z(3z^4+108-131z^2)r^2 + 1248z^5 + 4344z - 6456z^3 \tag{3.2d}$$

$$u_r^{\mathrm{poly}} = -3r(z-1)(z+1)(5z^2-1)(r-1)^2(r+1)^2 \tag{3.2e}$$

$$u_\theta^{\mathrm{poly}}(r,z) = -\frac{1}{8}zr(r-1)(r+1)(-30r^4z^2+5r^4+33r^4z^4+8r^2z^4+8z^4) \tag{3.2f}$$

$$u_z^{\mathrm{poly}} = 6z(z-1)^2(z+1)^2(r-1)(r+1)(3r^2-1) \tag{3.2g}$$

For $m=1$, we calculated the polynomial solution:

$$\psi^{\mathrm{poly}}(r,z) = \frac{18}{7}rz(22+r^4-9r^2)(z^4-1)\cos(\theta) \tag{3.3a}$$

$$\mathrm{rhs}_\psi^{\mathrm{poly}}(r,z) = -\frac{1728}{7}rz(77-5z^2r^2-25r^2+15z^2-77z^4+25r^2z^4)\cos(\theta) \tag{3.3b}$$

$$\phi^{\mathrm{poly}}(r,z) = r(z-1)^2(z+1)^2(14-10r^2+7z^2+2r^4-5z^2r^2+r^4z^2)(r^2-1)\sin(\theta) \tag{3.3c}$$

$$\mathrm{rhs}_\phi^{\mathrm{poly}}(r,z) = -1152r(-278+310z^4+287r^2+294z^2-25r^4-108z^6+100r^2z^6 - 255z^2r^2+125r^4z^4-435r^2z^4-15r^4z^2)\sin(\theta) \tag{3.3d}$$

After numerically discretizing the polynomial forms obtained for rhs_ψ and rhs_ϕ, we used our Helmholtz/Poisson solver to obtain numerical solutions for ψ and ϕ. The relative errors

$$\epsilon_\psi = \frac{|\psi-\psi^{\mathrm{poly}}|}{\sup|\psi^{\mathrm{poly}}|}, \quad \epsilon_\phi = \frac{|\phi-\phi^{\mathrm{poly}}|}{\sup|\phi^{\mathrm{poly}}|} \tag{3.4}$$

are shown in the (r,z) plane as the lower surfaces of Figs. 6–8 for the $m=0$ and $m=1$ solutions given above, and also for an $m=2$ polynomial solution. These are of order $O(10^{-14})$, i.e. machine precision, and never exceed $O(10^{-12})$.

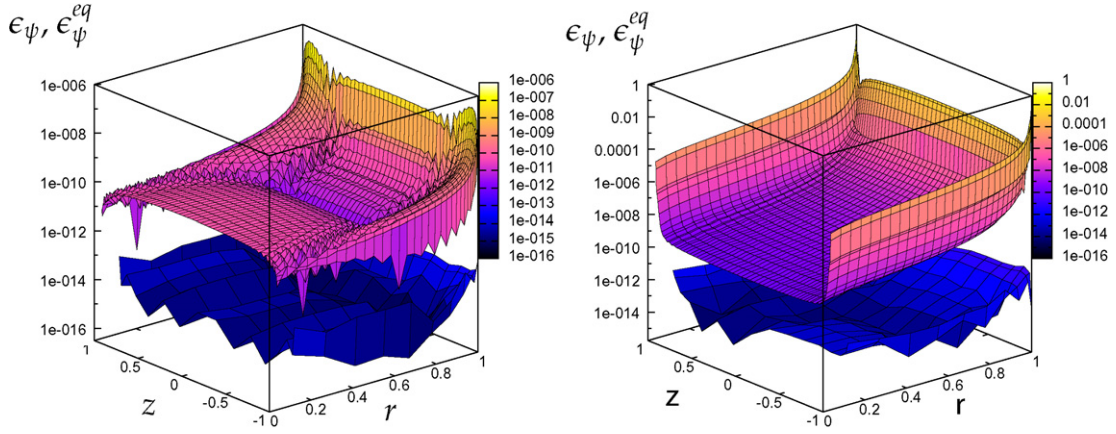

Fig. 6. Errors in ψ (left) and ϕ (right). Upper surfaces show the *a posteriori* error $\epsilon_\psi^{\mathrm{eq}}$, $\epsilon_\phi^{\mathrm{eq}}$ in satisfying the equations and defined in (3.5) for $m = 0$ after 100 timesteps of nested Stokes solver. Lower surfaces show the *a priori* relative error ϵ_ψ, ϵ_ϕ defined in (3.4) of the polynomial solution (3.2). Resolution used: $K = 64$, $N = 32$.

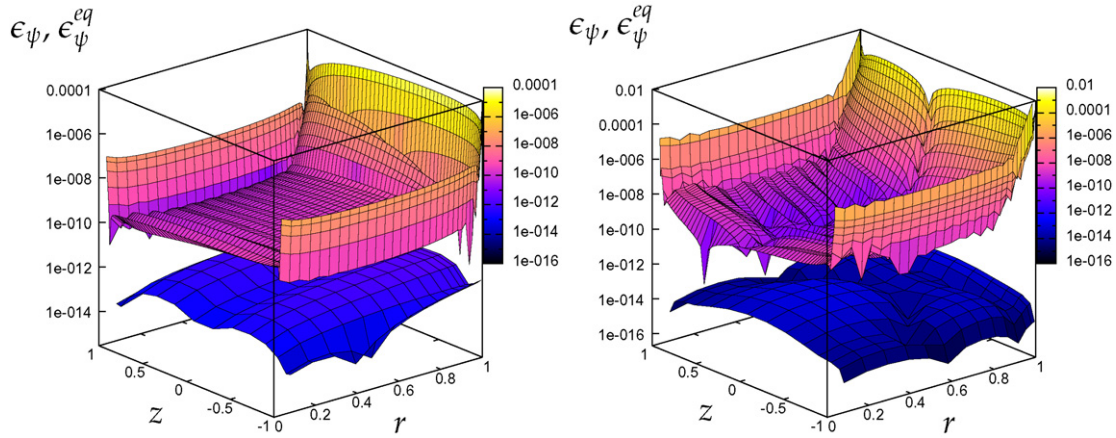

Fig. 7. Same as Fig. 6, for $m = 1$.

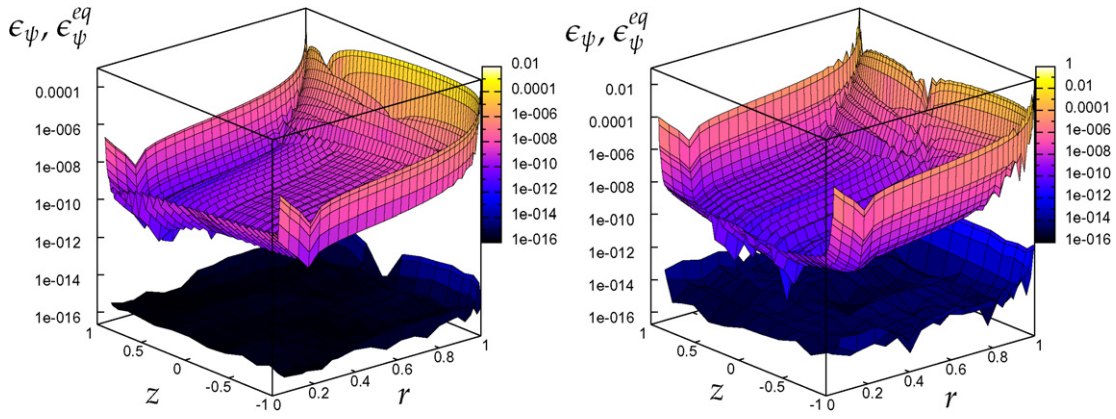

Fig. 8. Same as Fig. 6, for $m = 2$.

3.2. Non-polynomial solutions: error analysis

If the right-hand-sides rhs_ψ and rhs_ϕ are not polynomials that can be exactly represented within the spatial discretization, then the equations cannot be exactly satisfied. Note that the tau error introduced in favor of satisfying the boundary conditions at each level of the nested system of equations is necessarily propagated to the next level. That is, ψ^{n+1} is not an exact solution to the Poisson problem (2.13b) and in addition, the right-hand-side f_ψ is not an exact solution to the Helmholtz problem (2.13a). This implies that the error is not isolated in the equations corresponding to the highest wavenumbers, but is distributed among all the equations. However, we will see below that non-satisfaction of the equations for lower wavenumbers does not have severe consequences. In this subsection, as in the previous one, we restrict ourselves to the Stokes problem (3.1) whose errors behave like those of the Navier–Stokes equations.

Since no exact solution is available for comparison, we measure the *a posteriori* error in satisfying Eq. (3.1), defined as

$$\epsilon_\psi^{\mathrm{eq}} = \frac{|E\Delta_h\psi - \mathrm{rhs}_\psi|}{\sup|\mathrm{rhs}_\psi|}, \quad \epsilon_\phi^{\mathrm{eq}} = \frac{|E\Delta\Delta_h\phi - \mathrm{rhs}_\phi|}{\sup|\mathrm{rhs}_\phi|} \tag{3.5}$$

and shown as the upper surfaces of Figs. 6–8 in the physical (r,z) plane for the $m=0$, $m=1$ and $m=2$ modes. As is usually the case, the error is concentrated in the neighborhood of the boundaries, decaying rapidly away from them.

The errors (3.5) represent quite severe criteria, since these measure the satisfaction of the curl and double curl of the original equations; the error in satisfying the Stokes equations themselves is considerably lower, on the order of $\epsilon_\psi^{\mathrm{eq}}$ divided by $\mathrm{O}(K,N)$ and $\epsilon_\phi^{\mathrm{eq}}$ divided by $\mathrm{O}(K^2,N^2)$ near the boundary. This estimate relies on the fact that the spectrum of the error in satisfying the Stokes equations is approximately uniform, so that its derivatives are dominated by its high wavenumber terms.

The error depends significantly on the right-hand-sides rhs_ψ and rhs_ϕ. For arbitrary right-hand-sides, the boundary conditions can be very constraining and can lead to a nearly singular solution suffering from spurious oscillations, with an error near the boundary that is O(1). However, $\epsilon_\psi^{\mathrm{eq}}$, $\epsilon_\phi^{\mathrm{eq}}$ are considerably smaller when the right-hand-sides are calculated from the solution at the previous timestep, especially for the Stokes problem for which the nonlinear term is zero.

For the axisymmetric modes shown in Fig. 6, $\epsilon_\psi^{\mathrm{eq}}$ is $\mathrm{O}(10^{-6})$ on the boundaries and $\mathrm{O}(10^{-10})$ for the internal points. This is much less than $\epsilon_\phi^{\mathrm{eq}}$, which reaches O(1) at the cylinder corners. To understand this, we recall that in the axisymmetric case, the toroidal flow described by ψ is azimuthal and the poloidal flow described by ϕ is in the (r,z) plane. The azimuthal flow described by ψ follows smooth paths, while the flow described by ϕ must abruptly change direction near the corners. This poloidal flow in fact resembles the analytic asymptotic solution derived by Moffatt [37] for 2D flow in a rectangular container, which is weakly singular in that its vorticity behaves like $\rho^{1.74}$ (for a small distance ρ from the corner). This in turn implies that the axial component of the Laplacian of the Stokes equation measured by ϵ_ϕ diverges for exact solutions to the continuous 2D Stokes problem, in contrast with the numerically computed solution which is forced to be finite and regular. Satisfaction of the Stokes equation itself follows from the satisfaction of the boundary condition which our code imposes to precision $\mathrm{O}(10^{-14})$.

For the non-axisymmetric modes shown in Figs. 7 and 8, typical errors at the corners are O(0.01) for ψ and O(0.1) for ϕ and the same corner singularity is observed for both. This is because the 3D Stokes solutions are also weakly singular at the corners [38] and ψ and ϕ are coupled for $m \neq 0$. The relative error decreases rapidly away from the boundaries: it is $\mathrm{O}(10^{-4})$ only two gridpoints away and attains $\mathrm{O}(10^{-6})$ for the interior points.

The accuracy could be further enhanced – or confined to certain modes – by completing the method with the τ-correction [8,21,45], which takes into account the high-wavenumber residuals resulting from the imposition of the boundary conditions for each Helmholtz or Poisson problem.

3.3. Spectral convergence

The important indicator of spatial convergence for spectral methods is the decay rate of high-wavenumber coefficients in the solution fields. For a well-behaved solver, in the absence of volume and boundary singular-

ities, the magnitude of spectral coefficients should decay rapidly with wavenumber. For a laminar flow this decay rate should be exponential, but the presence of thin boundary layers can significantly influence the convergence. Figs. 9 and 10 show the spectral convergence for a full nonlinear Navier–Stokes simulation at $Re = 750$ at $T = 100\delta t = 1$ from initial conditions of $u_\theta = \omega_+(r)\, 2z/h$, $u_z = u_r = 0$. We show the (r, z) spectral coefficients for Fourier modes $m = 0$ and $m = 1$; those for higher m are similar. The convergence of the spectra can be qualified as quasi-exponential, meaning that the high-wavenumber spectral coefficients seem not to decrease below a level $O(10^{-12})$. This can almost certainly be attributed to the singular character of the solution to the Stokes equation near the cylinder corners. In support of this explanation, we note that the spectrum obtained after 100 timesteps of the linear (Stokes) solver behaves similarly, except for $\psi^{m=0}$, which displays true exponential decay, down to levels of 10^{-22} for the same resolution.

3.4. Axisymmetric rotor–stator configuration

The code was first tested on the well-documented axisymmetric rotor–stator configuration with aspect ratio $h = 2$. The first test is the reproduction of the characteristic steady state for $Re \approx 1850$ where the flow exhibits two recirculation bubbles (one large and the other much smaller) situated approximately at $(r = 0,\ z = 1/2)$ and $(r = 0,\ z = 0)$. The contour plot of the Stokes streamfunctions defined as

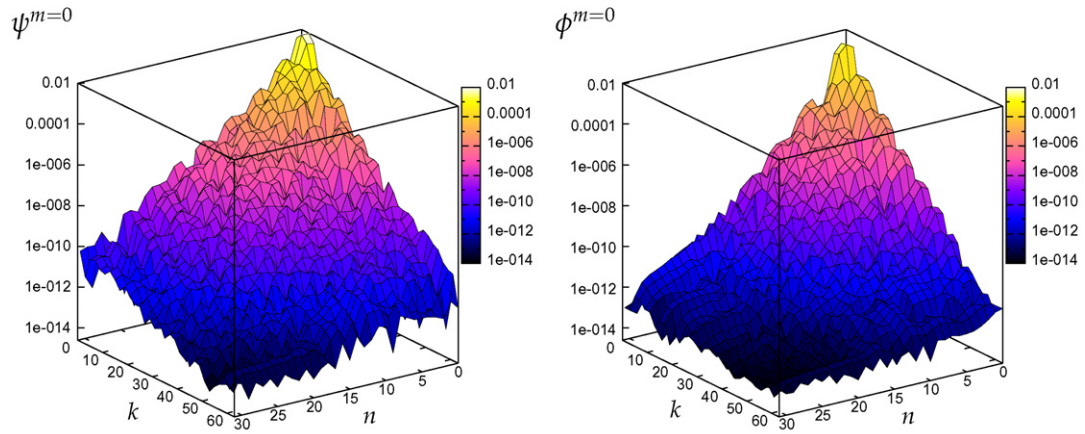

Fig. 9. Spectral coefficients for $m = 0$, after 100 timesteps of the nonlinear Navier–Stokes solver ($Re = 750$, $\delta t = 0.01$). Resolution used: $K = 64$, $N = 32$.

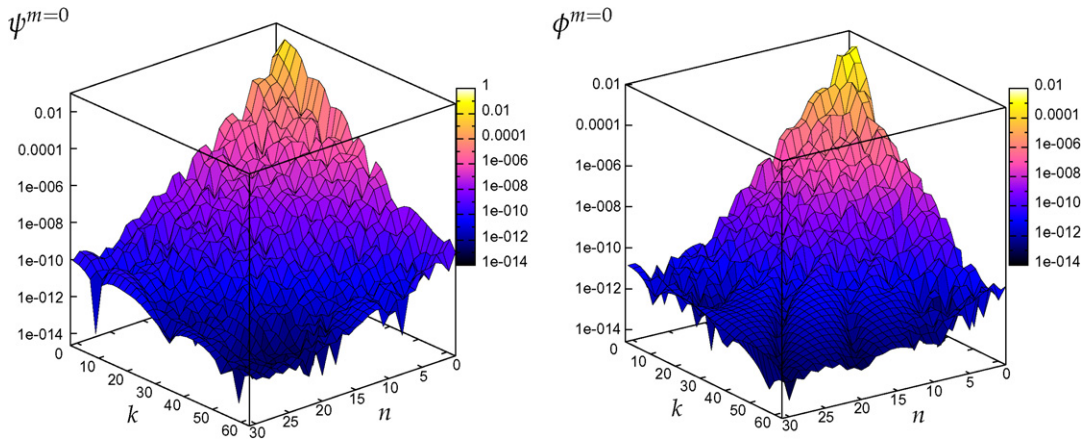

Fig. 10. Same as Fig. 9 for $m = 1$.

$$\sigma(r,z) = -r\partial_r\psi(r,z), \quad \eta(r,z) = -r\partial_r\phi(r,z) \tag{3.6}$$

presented in Fig. 12 matches that presented by Daube [6] (Fig. 11) and is similar to those of Lopez and Shen [7] obtained for the slightly larger aspect ratio $h = 2.5$. Quantitative agreement between our results and the previous calculations by Daube [6] and Lugt and Abbound [3] is established by comparing the profiles of axial velocity u_z on the cylinder axis (see Fig. 14). This test shows excellent agreement between our results obtained using the poloidal–toroidal formulation (Fig. 14(b)) and the velocity–vorticity formulation (Fig. 14(a)).

It was observed experimentally by Escudier [46] and numerically by Daube and Sorensen [4], Lopez [5], Daube [6], Gelfgat et al. [10] and Speetjens and Clercx [8] that this flow undergoes a Hopf bifurcation toward a flow oscillating at approximately 0.25 times the rotation frequency. Our computations produce this transition at Re near 2600 with a period of $T = 26.55$, within the ranges previously found for this configuration (see Table 3); deviations can probably be attributed to the differences in the regularization of the boundary con-

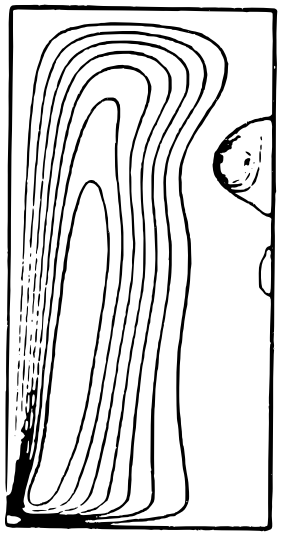

Fig. 11. Contours of Stokes poloidal streamfunction η from [6] for $Re = 1850$, $h = 2$.

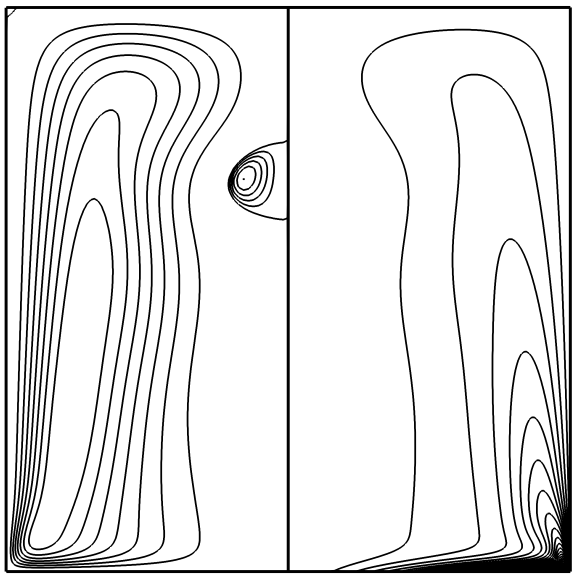

Fig. 12. Rotor–stator configuration for $Re = 1850$ and $h = 2$. Left: poloidal streamfunction η. Right: toroidal streamfunction σ.

Fig. 13. Rotor–stator configuration with $Re_c \approx 2150$ and $h = 3.5$. Isosurface $u_z \approx 0$ after subtraction of axisymmetric component.

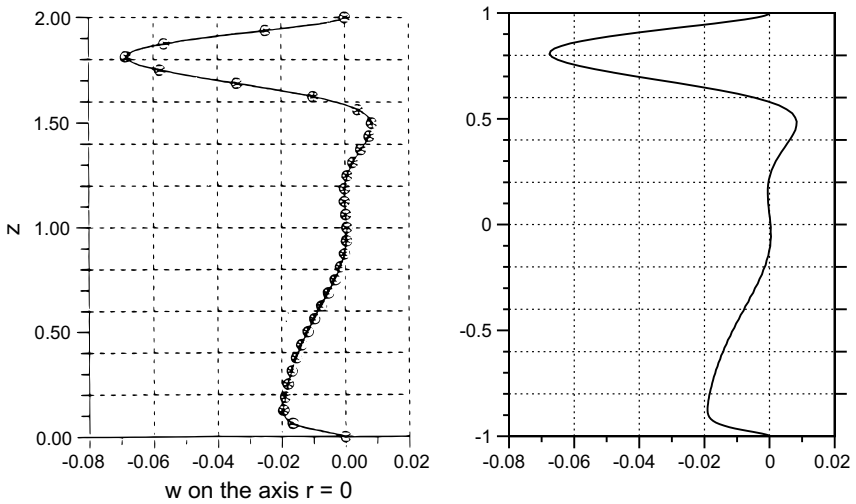

Fig. 14. Profile of u_z at $r = 0$ for rotor–stator configuration at $Re = 1850$, $h = 2$. (a) Profile from Daube [6]: results obtained using $\eta - \omega$ (∗) and $\mathbf{u} - \omega$ (∘) are superposed. (b) Profile at $t = 3000$ obtained from the present code, using poloidal–toroidal decomposition $\psi - \phi$.

Table 3
Oscillation period in rotor–stator configuration with $h = 2$ and $Re = 2800$

Method	Reference	T
$\mathbf{u} - \omega$	Daube [6]	25.52
$\eta - \omega$	Daube [6]	25.84
$\mathbf{u} - \omega$	Speetjens and Clercx [8]	26.61
$\mathbf{u} - p$	Gelfgat et al. [10]	≈26.7
$\psi - \phi$	This work	26.55

ditions. The simulation was performed with $\delta t = 0.01$ and with high spatial resolution $K \times N = 140 \times 70$ in order to well represent the sharp regularization profile corresponding to $\delta = 0.06$ imposed on the lateral boundary $r = 1$ (see Section 2.2) as proposed by Lopez and Shen [7] and also used by Speetjens [41]. The time evolution $u_\theta(r = 0.5, z = 0, t)$, along with the normalized power spectrum, are shown on Figs. 15–17.

3.5. First 3D instability

We have tested the non-axisymmetric aspects of the code using another rotor–stator configuration. For the aspect ratio of $h = 3.5$ we found that the first bifurcating mode has wavenumber $m = 3$ and critical Reynolds

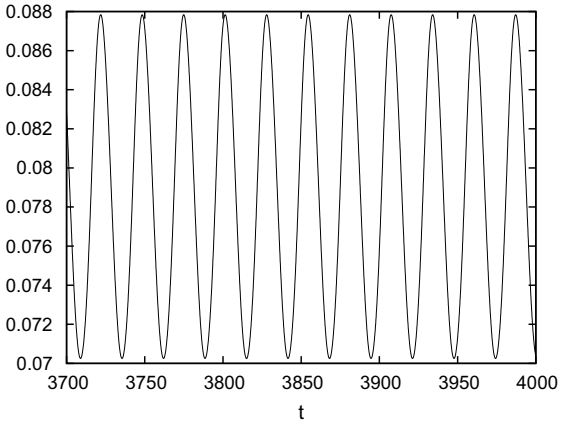

Fig. 15. Saturated state of time evolution of $u_\theta(r = 0.5, z = 0)$ for the rotor–stator configuration at $Re = 2800$, $h = 2$.

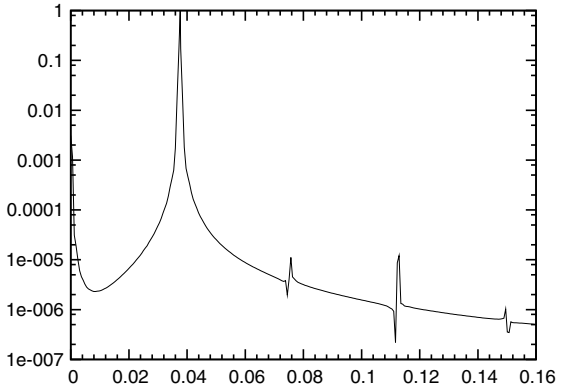

Fig. 16. Density power spectrum of $u_\theta(r = 0.5, z = 0)$ from Fig. 15.

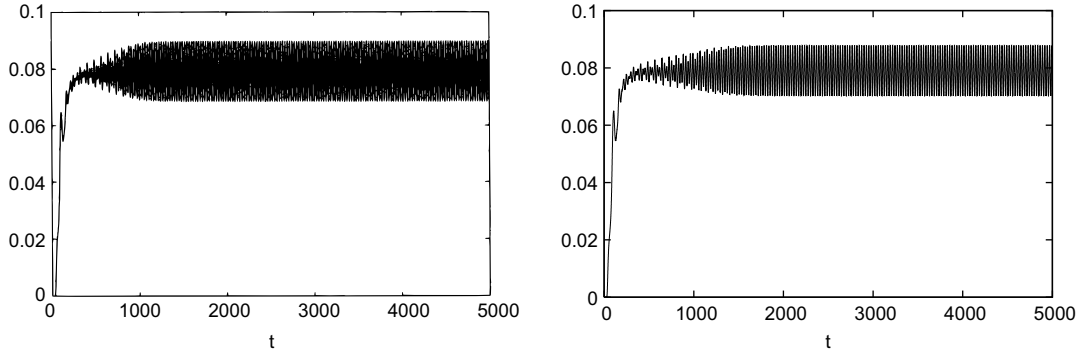

Fig. 17. Time history of $u_\theta(r = 0.5, z = 0)$ for the rotor–stator configuration at $Re = 2800$, $h = 2$. Left: from Speetjens and Clercx [8]. Right: current work.

number $Re_c = 2116$. This result is in good agreement with Gelfgat et al. [10], where the critical Reynolds number was estimated at $Re = 2131$. A characteristic spiral analogous to that visualized by Lopez et al. [14] for the same configuration is represented on Fig. 13.

4. Conclusion

Motivated by a need for a numerical tool adequate for investigating cylindrical von Kármán flow, we have written a spectral code which solves the Navier–Stokes equation for an incompressible fluid in a finite cylinder. This task encompasses a number of algorithmic challenges, which we list in order of decreasing difficulty. The first is to impose incompressibility, a goal which we achieved by using the poloidal–toroidal decomposition. In a finite cylinder, this formulation leads to differential equations of higher order and coupled boundary conditions [18,19]. In a companion paper [20], we described the way in which we used the influence matrix technique to transform these equations and boundary conditions into an equivalent set of decoupled Helmholtz or Poisson problems, each with Dirichlet boundary conditions.

The second challenge, which has been the main focus of this article, is the treatment of the cylindrical axis. The singularity engendered by the use of cylindrical coordinates is only apparent and should not be transmitted to the fields. We have dealt with the axis singularity by using a basis of radial polynomials developed by Matsushima and Marcus [22] which are analytic at the axis and which have properties similar to those of the Legendre polynomials. We have extended [22] in several ways. (i) The radial basis was developed for two dimensions, i.e. polar coordinates. Here, we have used it to represent fields in a three-dimensional cylinder of finite (non-periodic) axial length. This fairly straightforward extension was implemented by diagonalizing the differential operators in the axial direction. (ii) Numerical inaccuracy in the pseudo-spectral evaluation of the nonlinear term can generate terms which are not analytic. We have generalized to the high-order equations resulting from the poloidal–toroidal decomposition the procedure developed by Matsushima and Marcus [22] to avoid this problem. Care must be taken to preserve order and parity at each stage of the calculation. (iii) Differential operators expressed in this basis can, as in most such cases [31], be reformulated as recursion relations, which can be used to reduce the time for action or inversion of differential operators. Using the Sherman–Morrison–Woodbury formula, we have formalized the stable algorithm given in [22] for solving Poisson and Helmholtz problems in a time proportional to the number or radial gridpoints or modes.

The third challenge posed by a finite cylinder is the genuine singularity at the corners of the domain, where the disks and the cylinder which bound the domain meet. Finite difference and finite element codes intrinsically smooth the singularity; in contrast, spectral expansions attempt to converge to the discontinuity, leading to spurious oscillations. In our code, we replaced the discontinuous boundary conditions by a profile on the disks which is steep but continuous as the corner is approached. The geometrical singularity remains, but it is weak and does not prevent spectral convergence.

Tests performed for analytic polynomial solutions to the Helmholtz problem with an appropriate right-hand side showed that the solver reproduces exact solutions to nearly machine precision. For a non-polynomial solution, the solver displays exponential convergence of spectral coefficients of the solution. The potential equations (corresponding to the curl and double curl of the Navier–Stokes equations) are satisfied, with an error of only $O(10^{-10})$ for the interior points. The numerical code was parallelized using the MPI protocol. This made it possible to simulate nearly turbulent flow for $Re = 5000$ with a spatial resolution of $128 \times 160 \times 90$.

Finally, we have validated the hydrodynamic code by testing it against well-documented problems in the literature, demonstrating the feasibility of calculating solutions to the time-dependent Navier–Stokes equations in a finite cylindrical geometry which are both analytic and divergence-free.

Acknowledgements

The simulations reported in this work were performed on the IBM Power 4 of the Institut de Développement et des Ressources en Informatique Scientifique (IDRIS) of the Centre National de la Recherche Scientifique (CNRS) as part of Project 1119. P.B. was supported by a doctoral and post-doctoral grant from the Ecole Doctorale of the Ecole Polytechnique and the Ministère de l'Education Nationale, de la Recherche et de la Technologie (MENRT).

References

[1] T. von Kármán, Über laminare und turbulente Reibung, Z. Angew. Math. Mech. 1 (1921) 233–252.
[2] G.K. Batchelor, Note on a class of solutions of the Navier–Stokes equations representing rotationally-symmetric flow, Q. J. Mech. Appl. Maths. 4 (1951) 29.
[3] H.J. Lugt, M. Abboud, Axisymmetric vortex breakdown with and without temperature effects in a container with a rotating lid, J. Fluid Mech. 179 (1987) 179.
[4] O. Daube, J.N. Sorensen, Simulation numérique de l'écoulement périodique axisymétrique dans une cavité cylindrique, C.R. Acad. Sci. Paris 308 (1989) 463–469.
[5] J. Lopez, Axisymmetric vortex breakdown: Part 1. Confined swirling flow, J. Fluid Mech. 221 (1990) 533–552.
[6] O. Daube, Resolution of the 2D Navier–Stokes equations in velocity–vorticity form by means of an influence matrix technique, J. Comput. Phys. 103 (1992) 402–414.
[7] J. Lopez, J. Shen, An efficient spectral-projection method for the Navier–Stokes equations in cylindrical geometries – axisymmetric cases, J. Comput. Phys. 139 (1998) 308–326.
[8] M. Speetjens, H. Clercx, A spectral solver for the Navier–Stokes equations in the velocity–vorticity formulation, Int. J. Comput. Fluid Dyn. 19 (2005) 191–209.
[9] G. Gauthier, P. Gondret, M. Rabaud, Axisymmetric propagating vortices in the flow between a stationary and a rotating disk enclosed by a cylinder, J. Fluid Mech. 386 (1999) 105–126.
[10] Y. Gelfgat, P. Bar-Yoseph, A. Solan, Three-dimensional instability of axisymmetric flow in a rotating lid–cylinder enclosure, J. Fluid Mech. 438 (2001) 363.
[11] H.M. Blackburn, J.M. Lopez, Symmetry breaking of the flow in a cylinder driven by a rotating end wall, Phys. Fluids 12 (2000) 2698–2707.
[12] J.M. Lopez, F. Marques, J. Sanchez, Oscillatory modes in an enclosed swirling flow, J. Fluid Mech. 439 (2001) 109–129.
[13] C. Nore, M. Tartar, O. Daube, L.S. Tuckerman, Survey of instability thresholds of flow between exactly counter-rotating disks, J. Fluid Mech. 511 (2004) 45–65.
[14] J. Lopez, F. Marques, J. Shen, An efficient spectral-projection method for the Navier–Stokes equations in cylindrical geometries – three-dimensional cases, J. Comput. Phys. 176 (2002) 384–401.
[15] L. Marié, Transport de moment cinétique et de champ magnétique par un écoulement tourbillonnaire turbulent: influence de la rotation, Ph.D. thesis, Université Paris 7, 2003.
[16] F. Ravelet, L. Marié, A. Chiffaudel, F. Daviaud, Multistability and memory effect in a highly turbulent flow: experimental evidence for a global bifurcation, Phys. Rev. Lett. 93 (2004) 164501.
[17] R. Monchaux, M. Berhanu, M. Bourgoin, M. Moulin, P. Odier, J.-F. Pinton, R. Volk, S. Fauve, N. Mordant, F. Pétrélis, A. Chiffaudel, F. Daviaud, B. Dubrulle, C. Gasquet, L. Marié, F. Ravelet, Generation of a magnetic field by dynamo action in a turbulent flow of liquid sodium, Phys. Rev. Lett. 98 (2007) 044502.
[18] F. Marques, On boundary conditions for velocity potentials in confined flows: application to Couette flow, Phys. Fluids A 2 (1990) 729.
[19] F. Marques, M. Net, J. Massaguer, I. Mercader, Thermal convection in vertical cylinders. A method based on potentials, Comput. Methods Appl. Mech. Eng. 110 (1993) 157.
[20] P. Boronski, L.S. Tuckerman, Poloidal–toroidal decomposition in a finite cylinder: I. Influence matrices for the magnetohydrodynamic equations, J. Comput. Phys., doi:10.1016/j.jcp.2007.08.023.
[21] L. Tuckerman, Divergence-free velocity fields in nonperiodic geometries, J. Comput. Phys. 80 (1989) 403–441.
[22] T. Matsushima, P. Marcus, A spectral method for polar coordinates, J. Comput. Phys. 120 (1995) 365–374.
[23] S.A. Orszag, Numerical simulation of incompressible flows within simple boundaries: I. Galerkin (spectral) representations., Stud. Appl. Math. 50 (1971) 293–327.
[24] C. Canuto, M.Y. Hussaini, A. Quarteroni, T.A. Zang, Spectral Methods in Fluid Dynamics, Springer-Verlag, 1988.
[25] J. Boyd, Chebyshev and Fourier Spectral Methods, second ed., Dover, 2001.
[26] J. Boyd, N. Flyer, Compatibility conditions for time-dependent partial differential equations and the rate of convergence of Chebyshev and Fourier spectral methods, Comput. Methods Appl. Mech. Eng. 175 (1999) 370–411.
[27] S. Orszag, A. Patera, Secondary instsability of wall-bounded shear flows, J. Fluid Mech. 128 (1983) 347–385.
[28] V. Priymak, Y. Miyazaki, Accurate Navier–Stokes investigation of transitional and turbulent flows in a circular pipe, J. Comput. Phys. 142 (1998) 370–411.
[29] A. Leonard, A. Wray, A new numerical method for the simulation of three dimensional flow in a pipe, in: Proceedings of the Eighth International Conference on Numerical Methods in Fluid Dynamics, Springer-Verlag, 1982, pp. 335–342.
[30] W. Verkley, A spectral model for two-dimensional incompressible fluid flow in a circular basin, J. Comput. Phys. 136 (1997) 100–114.
[31] L. Tuckerman, Transformation of matrices into banded form, J. Comput. Phys. 84 (1989) 360–376.
[32] G. Georgiou, L. Olson, W. Schultz, The integrated singular basis function method for the stick-slip and the die-swell problems, Int. J. Numer. Methods Fluids 13 (1991) 1251–1265.
[33] L. Martin-Witkowski, J.S. Walker, Solutocapillary instabilities in liquid bridges, Phys. Fluids 14 (2002) 2647–2656.
[34] W. Schultz, N.-Y. Lee, J. Boyd, Chebyshev pseudospectral method for viscous flows with corner singularities, J. Sci. Comput. 4 (1989) 1–24.
[35] O. Botella, R. Peyret, Computing singular solution of the Navier–Stokes equation with the Chebyshev-collocation method, Int. J. Numer. Methods Fluids 36 (2001) 125–163.

[36] W. Dean, P. Montagnon, On the steady motion of viscous liquid in a corner, Proc. Camb. Phil. Soc. 45 (1949) 389.
[37] H. Moffatt, Viscous and resistive eddies near a sharp corner, J. Fluid Mech. 18 (1964) 1–18.
[38] C. Hills, H. Moffatt, Rotary honing: a variant of the Taylor paint-scraper problem, J. Fluid Mech. 418 (2000) 119–135.
[39] S. Nguyen, C. Delcarte, G. Kasperski, G. Labrosse, Singular boundary conditions and numerical simulations: lid-driven and thermocapillary flows, in: R. Savino (Ed.), Surface tension-driven flows and applications, Research Signpost, 2006, pp. 121–146.
[40] S. Nguyen, Dynamique d'une interface en présence d'une singularite de contact solide/fluide, Ph.D. thesis, Université Paris 11, 2005.
[41] M. Speetjens, Three-dimensional Chaotic Advection in a Cylindrical Domain, Ph.D. thesis, Eindhoven University of Technology, 2001.
[42] P.S. Marcus, Simulation of Taylor–Couette flow. I. Numerical methods and comparison with experiment, J. Fluid Mech. 146 (1984) 45–64.
[43] D. Haidvogel, T. Zang, The accurate solution of Poisson's equation by expansion in Chebyshev polynomials, J. Comput. Phys. 55 (1979) 115–128.
[44] P. Boronski, A Method Based on Poloidal–Toroidal Potentials Applied to the von Kármán Flow in a Finite Cylinder Geometry, Ph.D. thesis, Ecole Polytechnique, 2005.
[45] L. Kleiser, U. Schumann, Treatment of incompressibility and boundary conditions in 3D numerical spectral simulations of plane channel flows, in: E. Hirschel (Ed.), Proceedings of the Third GAMM Conference on Numerical Methods in Fluid Mechanics, Vieweg, 1980, pp. 165–173.
[46] M.P. Escudier, Observations of the flow produced in a cylindrical container by a rotating endwall, Exp. Fluids 2 (1984) 189.